Separation and Purification Technology 405 (2026) 138974

Contents lists available at ScienceDirect

Separation and Purification Technology

journal homepage: www.elsevier.com/locate/seppur

Tuning graphene oxide reduction in modified coarse filters for high-performance electrostatically assisted air filtration

Erwei Zhou [a,b,c], Jun Liu [g], Yang Gan [d,g], Lumin Chen [e], Ruijie Xie [a,b,c], Enze Tian [f,g,*], Jinhan Mo [a,b,c]

[a] Key Laboratory of Coastal Urban Resilient Infrastructures (Ministry of Education), College of Civil and Transportation Engineering, Shenzhen University, Shenzhen 518060, China
[b] State Key Laboratory of Subtropical Building and Urban Science, Shenzhen University, Shenzhen 518060, China
[c] Key Laboratory of Coastal Urban Soil-Water Environmental Evolution, Ministry of Ecology and Environment (under construction), Shenzhen University, Shenzhen 518060, China
[d] School of Physics and Materials Science, Guangzhou University, Guangzhou 510006, China
[e] Engineering Research Center of Biofilm Water Purification and Utilization, Technology of Ministry of Education, Anhui University of Technology, Ma'anshan 243032, China
[f] Dongguan Institute of Materials Science and Technology, Chinese Academy of Sciences, Dongguan 523808, China
[g] Songshan Lake Materials Laboratory, Dongguan 523808, China

ARTICLE INFO

Editor name: V Tarabara

Keywords:
Particulate matter
Fibrous filtration
Low pressure drop
Graphene oxide
Electrostatic

ABSTRACT

Airborne fine particulate matter (PM) poses a major threat to global public health and advanced manufacturing industries, including semiconductors, integrated circuits and biopharmaceuticals, making efficient airborne PM removal a fundamental necessity. However, conventional air filters face a critical trade-off between achieving high filtration efficiency and maintaining a low pressure drop. Although electrostatically assisted air (EAA) filtration can efficiently reduce the pressure drop, its filtration efficiency remains limited because the low relative dielectric constant (ε_r) of the fiber surface results in insufficient induced charges. Here, we propose a polyethylene terephthalate (PET) coarse filter modified with high-ε_r reduced graphene oxide (rGO) *via* a polydopamine (PDA)-mediated *in situ* coating. The ε_r and conductivity of the PDA/rGO@PET composite filters were precisely tuned through hydroiodic acid vapor reduction. Critically, we find that over-reduction renders the coating electrically conductive, inducing electric-field shielding that weakens the internal electric field and degrades filtration performance, establishing high resistance as a key design constraint. Under optimized reduction time (2.5 min), applying external voltages increased the filtration efficiency for 0.3–0.5 μm PM from 4.92% to 99.94%, while maintaining an ultralow pressure drop of 1.4 Pa at an air velocity of 0.053 m s^{-1}. This study provides a practical route for designing EAA filtration materials that simultaneously achieve high filtration efficiency and long-term operational stability while maintain ultralow pressure drop for airborne PM removal.

1. Introduction

Fine particulate matter ($PM_{2.5}$, aerodynamic diameter $\leq$ 2.5 μm) is recognized as one of the most critical environmental threats to global public health and to semiconductor manufacturing [1,2]. Despite extensive control measures, the global health burden attributable to $PM_{2.5}$ continues to increase [3]. Recent findings suggest that even long-term exposure to low concentrations of $PM_{2.5}$ is associated with increased mortality [4]. Globally, an estimated 3.9 million deaths in 2019 were attributable to long-term exposure to ambient $PM_{2.5}$ pollution [5]. Given that people spend near 90% of their time indoors [6], and that PM can infiltrate indoor environments through ventilation systems [7] and building envelopes, the development of efficient airborne PM filtration technologies is regarded as an essential requirement [8]. At the same time, air quality in semiconductor cleanrooms directly affects product quality, yield, and reliability [9], further underscoring the importance of efficient air filtration.

In general, PM capture relies on mechanical mechanisms, including Brownian diffusion, impaction, and interception [10]. However, improving filtration efficiency by amplifying these effects often leads to

* Corresponding author at: Dongguan Institute of Materials Science and Technology, Chinese Academy of Sciences, Dongguan 523808, China.
E-mail address: tianenze@dimst.ac.cn (E. Tian).

https://doi.org/10.1016/j.seppur.2026.138974
Received 2 April 2026; Received in revised form 10 June 2026; Accepted 16 June 2026
Available online 17 June 2026

higher pressure drop and lower PM holding capacity. For example, a commercial filter with an initial filtration efficiency of 88% for 0.3 μm PM exhibits an initial pressure drop of 11.3 Pa at 0.1 m s^{-1}, while it rises significantly to 250 Pa after accumulating 9.5 g m^{-2} PM [11]. Similarly, multilayer micro−/nanofiber filters can achieve filtration efficiency as high as 99.61%, but with a high pressure drop of 148 Pa at 15.83 cm s^{-1} [12].

Electrostatic assistance can enhance filtration efficiency by increasing the migration velocity of PM toward the fibers [13]. Synergistically charging both PM and fibers achieves superior performance compared with filtration methods relying solely on PM or fiber-charged mechanisms, as the Coulombic force between PM and fibers significantly exceeds the dielectrophoretic force [14]. Therefore, electrostatically assisted air (EAA) filtration has emerged as a promising approach to overcome the filtration efficiency-pressure drop trade-off. In EAA filtration, airborne PM is charged *via* corona discharge while the filter medium is polarized by an external electric field, enhancing PM capture without significantly increasing airflow resistance. The filtration efficiency for 0.3–0.5 μm PM of a polyethylene terephthalate (PET) coarse filter can be increased from 0.4% to 99% *via* EAA filtration [15]. Coating the fiber surface with materials of a larger relative dielectric constant (ε_r) can further improve the induced charge density during polarization, and therefore enhance the filtration efficiency [16]. For example, Tian et al. loaded ZnO onto the polyurethane (PU) filter and achieved a filtration efficiency of 87.0% for 0.3 μm PM at an air velocity of 1.1 m s^{-1} with a pressure drop of 3.8 Pa [16]. Gao et al. achieved a filtration efficiency of 90.50% for 0.3 μm PM by loading MnO_2 onto the PU filter at an air velocity of 1 m s^{-1} with a pressure drop of 13.0 Pa [17]. Therefore, improving the dielectric properties of the material can enhance its filtration efficiency (ZnO: 9.9 [16], MnO_2: 10.85 [17]). Nevertheless, the ε_r values of these coatings are relatively low, limiting the amount of induced charges and thus the achievable filtration performance compared to that of high-efficiency particulate air filters.

Graphene oxide (GO) is a two-dimensional, atomic-layer-thin carbon material with high specific surface area and abundant oxygen-containing functional groups [18,19], and is widely used in sensors [20], membrane separation [21,22], and energy storage [23]. Compared with conventional polymers, GO exhibits extremely high ε_r with reported values ranging from 2 to 10^6 [24]. For example, Verdejo et al. demonstrated that uniform GO coverage on a polymer matrix effectively enhanced its ε_r [25]. The ε_r increases from 27.93 for water-soluble polypyrrole/polyvinyl alcohol blend to 155.18 for nanocomposites with 3 wt% GO loading [26]. Following reduction to reduced graphene oxide (rGO), the oxygen-containing functional groups can be removed, and the material becomes conductive [20]. This transition from dielectric GO to conductive rGO enhances the ability to sustain induced charges under an electric field, thereby strengthening electrostatic interactions with charged PM.

In this work, we integrate a PDA-mediated GO coating on the surface of PET coarse filters, followed by controlled hydroiodic acid (HI) vapor reduction, to construct high-ε_r and conductive surfaces in EAA filters aimed at achieving high filtration efficiency and long-term operational stability while maintaining ultralow pressure drop. By systematically investigating the effects of HI reduction time, particle charging voltage, filter polarization voltage, air velocity, and operational duration, we elucidate the underlying mechanisms that govern the trade-off between filtration efficiency and airflow resistance. Importantly, we discover that over-reduction of GO renders the fiber coating electrically conductive, inducing electric-field shielding that counterproductively weakens the internal electric field, identifying high resistance of the high-ε_r coating as a critical and previously unreported design constraint. This study establishes a comprehensive framework for designing advanced filtration media through precise control of surface chemistry and electrical properties, offering a promising pathway toward energy-efficient and environmentally friendly air purification technologies.

2. Materials and methods

2.1. Design of electrostatically responsive fibers

To minimize the air pressure drop, a PET coarse filter with high porosity (air permeability ≥3000 L m^{-2} s^{-1}) and large pore size was selected as the substrate. Compared with dense membranes, such coarse filters provide deeper filtration pathways and higher dust holding capacity, thereby reducing the risk of clogging [27]. Since pristine PET has a low ε_r, it is designed to be modified with high-ε_r coatings to enhance charge induction during polarization. Here, PDA was chosen as an interfacial mediator because PET fibers and GO sheets are both negatively charged [28,29], making direct GO deposition electrostatically unfavorable. PDA can spontaneously polymerize *in situ* and conformally deposit as an ultrathin, positively charged layer on virtually any substrate, thereby enabling strong electrostatic attraction toward negatively charged GO while also increasing surface area and the density of active binding sites [30]. GO was incorporated for its high ε_r [24]. Upon chemical reduction, GO is converted to rGO, which further enhances ε_r for stronger charge induction.

In an EAA filtration module, PM is first charged and then passes through the polarized PDA/rGO@PET filters. Comparing Fig. 1a and b, the introduction of EAA strengthens electrostatic interactions between PM and fibers, thereby increasing the probability of capture. Increasing ε_r of the filter can enhance the intensity of the induced electric field, and thereby strengthen electrostatic forces and improve PM capture efficiency (Fig. 1b–d). Due to the high ε_r of PDA and rGO, the coated fibers generate substantial induced charges in an electric field. These induced charges lead to strong electrostatic interactions with charged PM, enabling highly efficient PM capture.

2.2. Preparation of PDA/rGO@PET filters

Commercial PET coarse filters (diameter: 50 mm, thickness: 7 mm) were used as substrates. As shown in Fig. 2, the filters were immersed in 60 mL of 10 mM Tris buffer solution (Merck Life Science Co., Ltd., pH = 8.5) and stirred at 200 rpm for 30 min at 25 °C. Subsequently, 140 mg of dopamine hydrochloride (DA, Aladdin Industrial Co., Ltd.) was added, and the mixture was stirred at 200 rpm for another 30 min to initiate *in situ* polymerization. Then, 3 mL of GO dispersion (nanosheet diameter < 500 nm, 2 mg mL^{-1}, Xianfeng Nanomaterials Technology Co., Ltd.) was introduced and the reaction continued for 24 h under stirring at 200 rpm, 25 °C. After reaction, the samples were washed four times with deionized water and once with ethanol, then dried in an oven at 60 °C for 3 h to obtain PDA/GO@PET filters.

For the reduction step, the PDA/GO@PET filters were placed above a

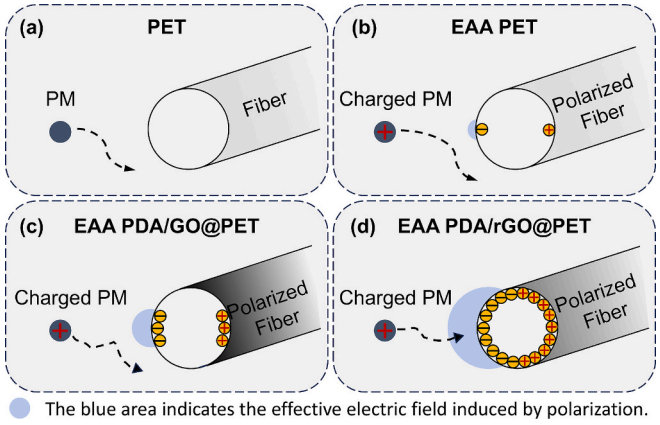

Fig. 1. Schematic illustrating the interaction between a PM and a (a) PET, (b) PDA@PET, (c) PDA/GO@PET, and (d) PDA/rGO@PET fiber in an EAA filtration module.

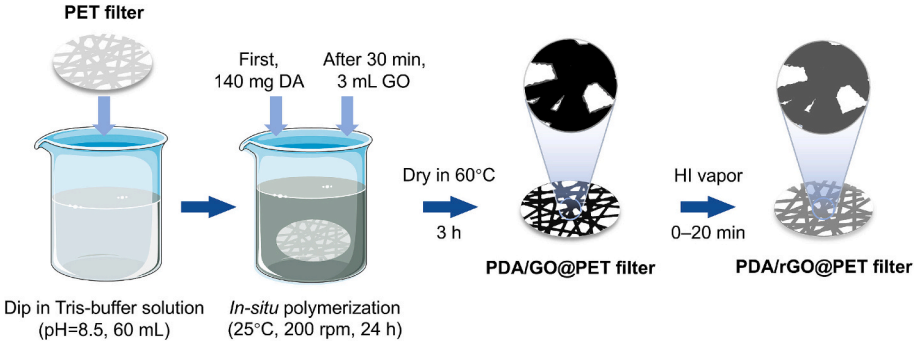

Fig. 2. Schematic illustration of the preparation methods of PDA/GO@PET and PDA/rGO@PET filters.

glass dish containing HI solution (Merck Life Science Co., Ltd.), allowing HI vapor to contact the GO coating. The reduction times were set at 0, 2.5, 5, 10, and 20 min to prepare PDA/rGO@PET filters with different reduction levels. Then, they were dried in an oven at 60 °C for 3 h, and denoted as PDA/rGO@PET-0, −2.5, −5, −10 and − 20 min filters.

2.3. Characterization and performance tests

The morphology and composition of the filters were analyzed by an optical microscope (BX53M, Olympus Co., Ltd., Japan), a field emission scanning electron microscope (FESEM, Verios 5UC, ThermoFisher, USA), and an energy dispersive X-ray spectrometer (EDS) for elemental mapping. The square resistances of the rGO with different reduction times were measured using a resistance gauge (RM3544–01, HIOKI EE Corporation, Japan). The detailed experimental and testing procedures are presented in Supplementary **Methods S1.** The filters (diameter: 10 mm) were pressed into thin sheets using a roll squeezer and then placed in a broadband dielectric impedance spectrometer (Novocontrol CONCEPT 40 model, Germany) to measure ε_r of the filters over a frequency range of 1 Hz to 10^5 Hz [31]. Direct measurement of uncompressed samples is not feasible due to the extremely high porosity of the filter materials (98.8%–99.3% [32]), in which the overwhelming air fraction ($\varepsilon_r \approx 1$) would dominate the dielectric response and render fiber-level differences undetectable. Compression was therefore a deliberate step to reduce the air-gap contribution and improve measurement sensitivity. The compression degree was kept consistent across all samples by controlling the compressed thickness to 0.5 mm, ensuring valid and reproducible comparisons between samples. Currently, we do not have access to instrumentation capable of directly measuring the ε_r and conductivity of a single fiber. The reported values thus serve only as a semi-quantitative indicator of the change in dielectric and conductive properties before and after surface modification.

Filtration performance was evaluated using a laboratory-scale EAA filtration setup (Fig. 3). Two DC high-voltage power supplies (71734P and 73030P Boer Co., Ltd., China) were employed: one for PM charging (Zone 1, U_c represents charging voltage) and the other for filter polarization (Zone 2, U_p represents polarization voltage). Positive corona discharge was adopted for PM charging because it generates significantly less ozone as a by-product compared to negative corona [33]. U_c was varied from 0 to 11 kV for experiments and 20 kV was chosen as the upper representative U_p to ensure safe operation below the experimentally observed breakdown threshold (~25 kV). Ambient indoor PM was used as the loading pollutant, with its size distribution shown in Supplementary **Fig. S1**. The number concentrations of PM (0.3 μm to 3 μm) upstream and downstream of the filter were monitored using a particle counter (Aerotrak PC 9306, TSI Inc., USA) with a sampling period of 45 s and a 2 min switching interval between the upstream and downstream measurements. The number concentrations of ambient PM are approximately 41,384 pcs L^{-1} at 0.42 m s^{-1} and 7170 pcs L^{-1} at 0.053 m s^{-1}. Air pressure drop was measured across the filter using a differential pressure gauge (DP-CALC 5825, TSI Inc., USA) [34]. The filtration velocity was measured at the exhaust using an air velocity meter (VELOCICALC 9535-A, TSI Inc). Filtration efficiency, quality factor (QF), and comprehensive quality factor (CQF) were calculated according to equations provided in Supplementary **Methods S2**. The calculation method for standard error of the mean (SE) was provided in

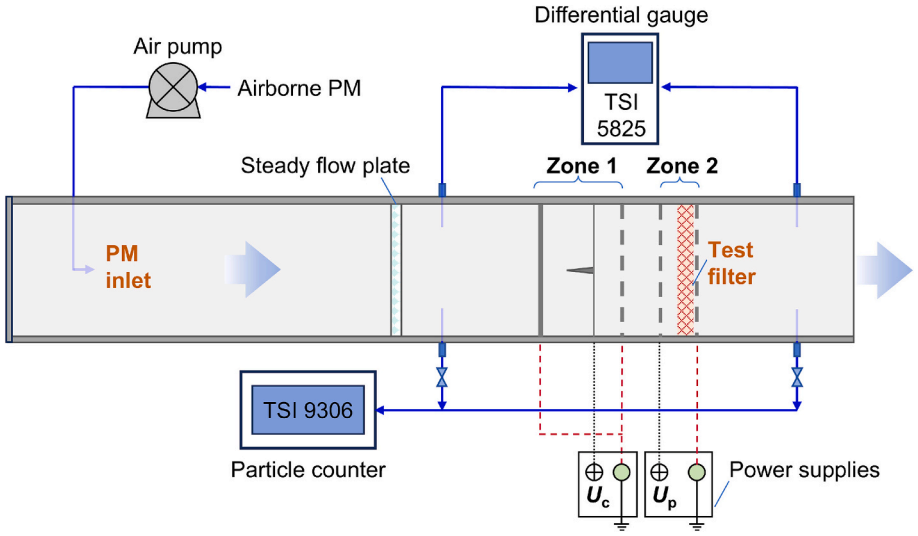

Fig. 3. Schematic illustration of the EAA filtration setup for performance test.

Supplementary **Methods S2**.

3. Results and discussion

3.1. Filter characterizations

Fig. 4 shows photographs and SEM images of the pristine PET filter and the PDA/rGO@PET filters reduced for 2.5 min (denoted as PDA/rGO@PET-2.5 min). The PET coarse filter exhibits a loose, highly porous fibrous network, which maintains open flow pathways even after the coating process (Fig. 4a–c). As shown in Supplementary **Fig. S2a,** the pristine PET fibers appear white. After deposition of PDA and GO, the fiber surface became dark grey (Supplementary **Fig. S2b–c**), and it became slightly lighter after being reduced by HI vapor (Supplementary **Fig. S2d**). Compared to the pristine PET filter, the PDA/rGO@PET filter shows a roughened fiber surface while preserving the inter-fiber gaps (Fig. 4d–e). The appearance of sheet-like rGO and granular PDA structures on the fiber surface indicates successful surface functionalization (Fig. 4f). Notably, PDA likely promotes adhesion between rGO and PET, which may suppress coating detachment during handling and operation. Elemental mapping by EDS (Fig. 4g) further verifies the spatially uniform distribution of the coatings.

3.2. Influence of PDA and (r)GO coating on the filtration performance of PET filter

The obtained filters, including pristine PET, PDA@PET, PDA/GO@PET, and PDA/rGO@PET, were installed in the EAA filtration device to evaluate their filtration performance (Fig. 3). In order to demonstrate the repeatability of the filters, two samples with the same modification were used and tested with voltages ($U_c = 9$ kV and $U_p = 20$ kV) off or on. Their single-pass filtration efficiency for 0.3–0.5 μm PM at air velocity of 0.42 m s^{-1} are summarized in Fig. 5**.** In each graph, bars of the same color represent the same material tested under the same voltage condition (either off or on), with the two adjacent bars of identical color corresponding to two independent samples of that material tested under identical conditions to assess measurement repeatability. As shown in Fig. 5a, the filtration efficiency for 0.3–0.5 μm PM of the pristine PET filters increased from 2.03% to 75.37% when both U_c and U_p were applied. Under the same voltages and air velocity, the average filtration efficiency increased from 1.74% to 93.74% for the PDA@PET filters (Fig. 5b) and from 2.54% to 94.16% for the PDA/GO@PET filters (Fig. 5c). This demonstrates that the PDA and GO coating significantly enhances the filtration efficiency of the material. After 2.5-min reduction of GO, the PDA/rGO@PET-2.5 min filters achieved the highest average efficiency of 95.93% (Fig. 5d). The improvement in filtration efficiency from PDA@PET (93.74%) to PDA/rGO@PET-2.5 min (95.93%) is nonetheless practically meaningful as the penetration rate decreased from 6.26% to 4.07% (a 35.0% reduction), and the QF improved from 0.16 to 0.18 Pa^{-1} (a 12.5% improvement). Furthermore, 95% represents a critical threshold in standard filtration grade classifications [35], so achieving 95.93% efficiency constitutes an advancement to the next performance grade.

To interpret the above performance differences, we associate the filtration efficiency results with the EAA working principle (Fig. 1) and the experimentally measured ε_r of the coated filters (Supplementary **Fig. S3**). The results correlated well with the predictions shown in Fig. 1. As shown in Supplementary **Fig. S3**, ε_r values of the pristine PET, PDA@PET, PDA/GO@PET, and PDA/rGO@PET filters were respectively 2.18, 2.22, 2.37 and 2.56 at 10^3 Hz. It should be noted that the overall ε_r of the fiber filter is dominated by the large air fraction due to the extremely high porosity of the coarse fiber material (98.8–99.3% [32]), such that the small amount of high-ε_r material loaded on the fiber surface cannot substantially elevate the bulk ε_r of the filter. Therefore, the reported ε_r values serve as semi-quantitative indicators of the change in dielectric properties before and after surface modification rather than absolute measures of the fiber-level ε_r. The actual increase in ε_r at the fiber surface is likely substantially greater than the bulk measurements

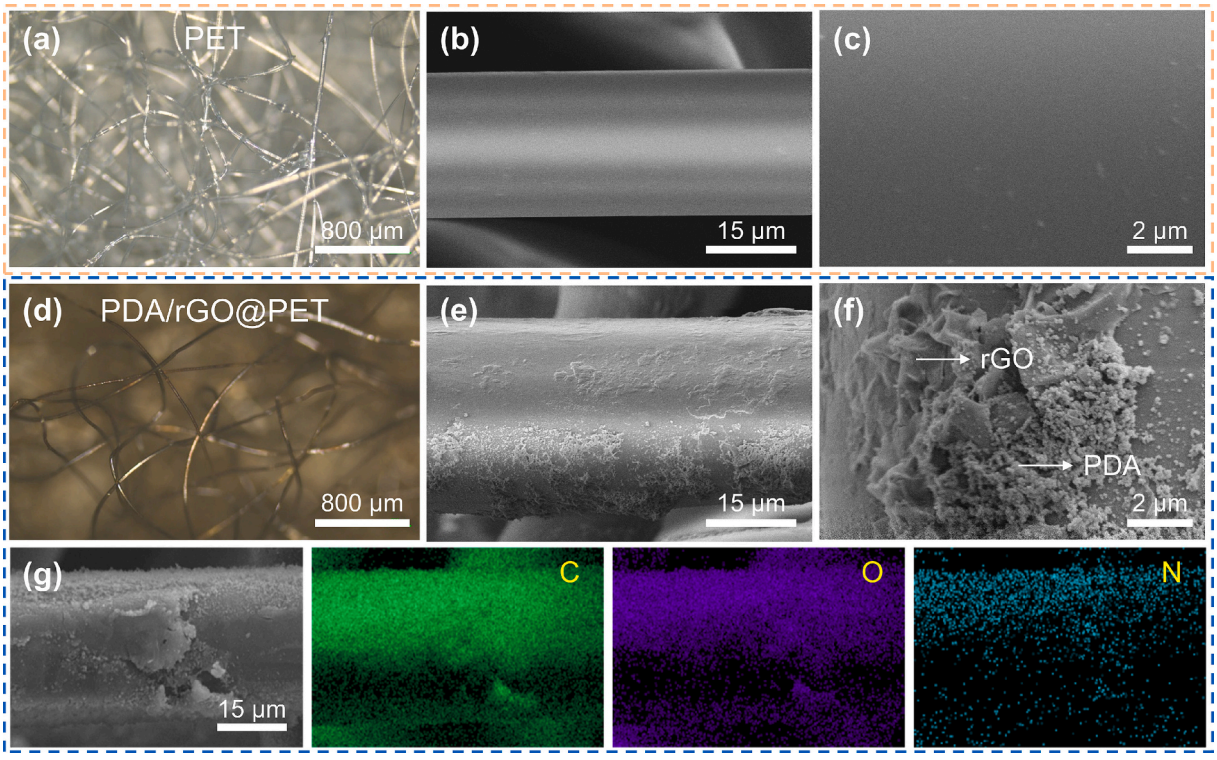

Fig. 4. Milli-micro-nano scale morphologies of pristine PET and PDA/rGO@PET-2.5 min filters. (a) Optical microscope image and (b)–(c) SEM images of the pristine PET filter. (d) Optical microscope image and (e)–(f) SEM images of the PDA/rGO@PET-2.5 min filter. (g) SEM image and corresponding EDS elemental mapping images of a fiber in PDA/rGO@PET-2.5 min filter.

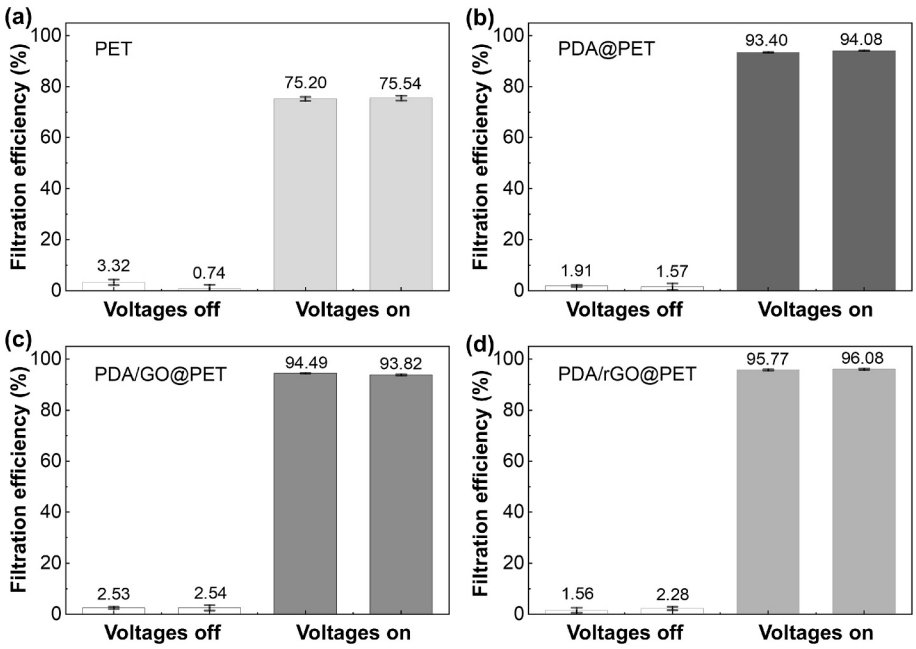

Fig. 5. Filtration efficiency at air velocity of 0.42 m s^{-1} for 0.3–0.5 μm PM of (a) pristine PET, (b) PDA@PET, (c) PDA/GO@PET and (d) PDA/rGO@PET-2.5 min filters with voltages (U_c = 9 kV and U_p = 20 kV) off or on. Error bars represent the SE from four independent measurements.

suggest. Nevertheless, the progressive increase in ε_r after PDA/GO and PDA/rGO modification is consistent with the observed enhancement in EAA filtration efficiency.

From the previous text, we learned that GO has different ε_r at different reduction states, which may also affect the filtration performance of the material. Motivated by this dependence, we further optimized the PDA/rGO@PET filters by varying the HI-vapor reduction time and evaluating the resulting filtration performance. As shown in Fig. 6a, with the increase of reduction time, the filtration efficiency first increased and then decreased. Under 2.5 min of reduction, the filtration efficiency reached its peak at 95.93%. Therefore, both the ε_r and electrical conductivity of the fiber coating jointly govern filtration efficiency. A higher ε_r enhances the induced charge and strengthens the electric field within the filter, while an excessive increase in conductivity promotes charge carrier mobility along the fiber surface, leading to electric-field shielding that diminishes electrostatic particle capture. Due to the difficulty in measuring the electrical conductivity of GO and rGO loaded on fiber surfaces, we spin-coated GO and rGO nanosheets onto silicon wafers to measure their square resistance. As shown in Fig. 6b, when the reduction time increases, the square resistances of the rGO decrease exponentially. Together with the bulk ε_r measurements of the composite fibers, these conductivity data provide a semi-quantitative basis for tracking the competing contributions of conductive shielding as a function of reduction degree.

Taken together, these results suggest a trade-off governed by two competing mechanisms. On one hand, a higher ε_r promotes dielectric polarization of the fiber surface, increasing the induced charge density and intensifying the local electric field that drives electrostatic particle capture (Fig. 6c and d). On the other hand, when the reduction time exceeds 2.5 min, the electrical conductivity of the rGO coating rises sufficiently to redistribute surface charges, effectively shielding the internal electric field (Fig. 6e), and reducing the electrostatic driving force for particle deposition. The optimal reduction time of 2.5 min represents the point at which dielectric enhancement is maximized before conductive shielding becomes dominant.

3.3. Influence of charging voltages on filtration performance

The PDA/rGO@PET-2.5 min filters, which delivered the highest filtration efficiency, were selected for performance evaluation under different conditions. As shown in Fig. 7a, when both U_c and U_p were turned off, the filtration efficiency for 0.3–0.5 μm PM was only 4.92%. Given that the inter-fiber gap was approximately 300 μm, PM lacking sufficient charge were less likely to approach the fibers closely during airflow passage, thereby reducing the possibility of effective PM capture.

When U_p = 0, increasing U_c increased the charge carried by PM. In this configuration, fibers remain electrically neutral, and the dominant electrostatic interaction is the image force between the charged PM and the neutral fiber surface [10]. There is a critical U_c, which is called the corona onset voltage of approximately 6 kV. When the U_c is lower than the corona onset voltage, the pin in zone 1 does not discharge and thus cannot effectively charge PM. Therefore, when U_c increased from 0 kV to 5 kV, the filtration efficiency increased slowly from 4.88% to 15.10%, but increased significantly from 15.10% to 60.30% when U_c increased from 5 kV to 7 kV. The filtration efficiency achieved its highest at 86.79% when U_c = 11 kV. Despite increasing particle charge, the absence of a long-range fiber field limits efficiency gains in this regime.

When U_p was turned on and set at 20 kV, the electric field polarized the fibers, generating a non-uniform field in the inter-fiber space. Even in the absence of particle pre-charging (U_c = 0 kV), neutral PM entering this non-uniform field experience a dielectrophoretic force [36,37], which polarizes the particles and draws them toward the fiber surface. This longer-range force accounts for the significant efficiency increase from 4.88% to 57.09% even at U_c = 0 kV. Further introducing a Coulomb force [38] between charged particles and polarized fibers by increasing U_c results in a synergistic enhancement, improving the filtration efficiency to 99.53%. This efficiency hierarchy dielectrophoretic force (neutral PM, polarized fiber) < image force (charged PM, neutral fiber) < Coulomb forces (charged PM, polarized fiber) directly explains the progressive efficiency improvement observed in Fig. 7a.

As U_c increased, QF remained relatively constant (about 0.15 Pa^{-1}) before U_c = 6 kV and then changed significantly when U_c = 7 kV. Ultimately, QF was increased to 0.91 Pa^{-1} at U_c = 11 kV (Fig. 7b). However, a higher U_c is not necessarily better performance, as it leads to higher energy consumption. As U_c increased, energy consumption rose far faster than filtration efficiency increased (Supplementary **Fig. S4**). The difference between the total power consumption curves at U_p = 20 kV and 0 kV yields the power consumed during electret formation

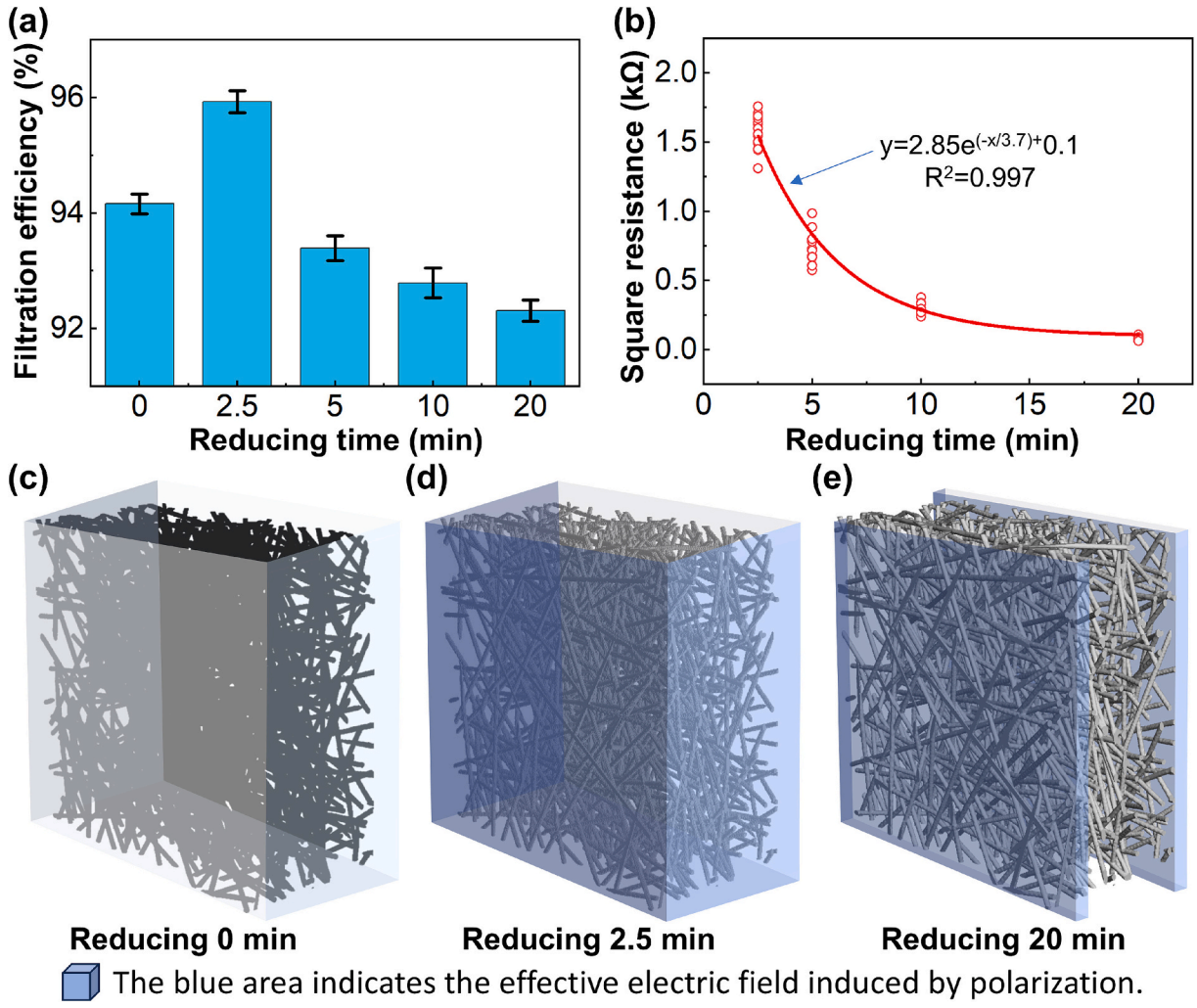

Fig. 6. (a) Filtration efficiency for 0.3–0.5 μm PM of PDA/rGO@PET filters with different reduction times. Error bars represent the SE from eight independent measurements. (b) Square resistances of GO coatings on silicon wafers with different reduction times. (c–e) Schematic illustrations of the effective electric fields for PM capture by PDA/rGO@PET filters with reduction time of (c) 0, (d) 2.5 and (e) 20 min.

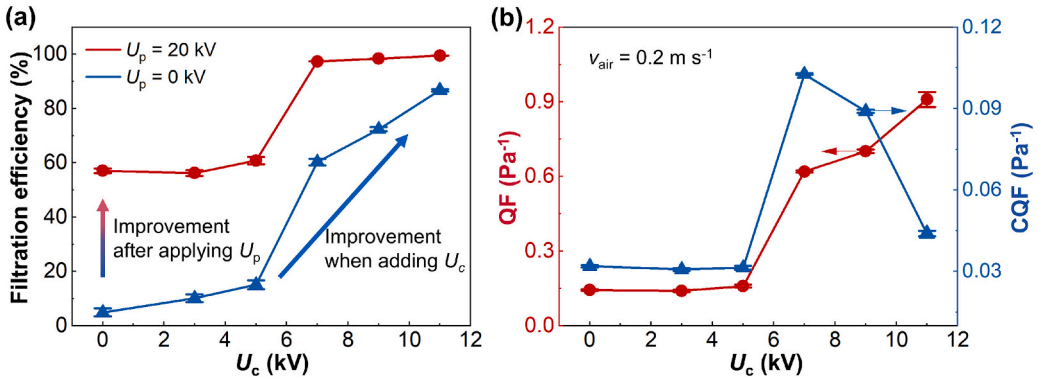

Fig. 7. Filtration performance of the EAA PDA/rGO@PET-2.5 min filter at different charging voltages. (a) Filtration efficiency for 0.3–0.5 μm PM at 0.2 m s^{-1} under different U_c and U_p. Error bars represent the SE from four independent measurements. (b) QF and CQF for 0.3–0.5 μm PM at 0.2 m s^{-1} under different U_c when U_p = 20 kV. Error bars represent the SE from four independent measurements.

(polarization). The total energy consumption and energy consumption due to particle charging and fiber polarization are 11.43, 4.79, and 6.64 W m^{-2}, respectively, when U_c = 9 kV and U_p = 20 kV.

To avoid overestimating the performance-cost ratio of the electrostatic filtration, the electrical power consumption is included in the CQF by assuming that the extra power consumption for efficiency improvement is equivalent to an extra equivalent pressure drop (Supplementary **Method S2**). Consequently, CQF reached its peak (about 0.103 Pa^{-1}) at U_c = 7 kV, and then dropped to 0.044 Pa^{-1} at U_c = 11 kV. Considering CQF achieving a high level (0.089 Pa^{-1}) and filtration efficiency

exceeding 98%, the optimal U_c was selected at 9 kV.

3.4. Performance evaluation under different conditions

Both 0.3 μm and larger PM should be considered for their single-pass filtration efficiency. For example, the primary size distribution of SARS-CoV-2 in droplet particles fell into 0.25–1 μm and above 2.5 μm [39]. The filtration efficiency of PDA/rGO@PET-2.5 min filters for 0.3–3 μm PM under different U_c and U_p was shown in Supplementary **Fig. S5**, which increased as the PM size enlarged. For example, the filtration efficiency for 0.3–0.5 μm PM and 1–3 μm PM were 98.40% and 98.61%, respectively, at U_c = 9 kV and U_p = 20 kV. To evaluate the filtration performance of PDA/rGO@PET-2.5 min filter under different air velocities, 0.053, 0.1, 0.2, and 0.45 m s^{-1} were selected [40,41]. Among these, 0.053 m s^{-1} is the standardized testing velocity specified in JG/T 404–2013 for filtration material. As can be seen from Fig. 8a and b, the filtration efficiency decreased from 99.94% to 95.99%, and the pressure drop increased from 1.4 Pa to 18.8 Pa as the air velocity rose from 0.053 m s^{-1} to 0.45 m s^{-1}. The electric field-mediated efficiency, obtained by subtracting the mechanical efficiency from the total efficiency, accounted for >90% of the total filtration performance (Fig. 7a). Therefore, the filtration efficiency trends presented in Fig. 8a essentially reflect the dependence of electric field-mediated efficiency on air velocity. High air velocities substantially reduce the residence time of particulate matter in the corona charging zone and the filter media, thereby decreasing filtration efficiency. At the air velocity of 0.053 m s^{-1}, the filtration efficiency reached its maximum of 99.94%, while the pressure drop was the minimum of 1.4 Pa. Notably, when the filter material is pleated into a device, the material-level filtration velocity of 0.053 m s^{-1} corresponds to frontal air velocities of 0.45–2 m s^{-1}, covering the operational range of typical HVAC and indoor air purification systems. At the maximum v_{air} = 0.45 m s^{-1} in this work, the Δp_a of the PDA/rGO@PET-2.5 min filter is 18.8 Pa. Considering the fan efficiency (η_{fan}) to be 0.71 [42], The energy consumption of fan (P_{fan}) is estimated as 11.90 W m^{-2} according to $P_{fan} = \Delta p_a\, v_{air}\, \eta_{fan}^{-1}$. Adding the energy consumption of power supplies (11.43 W m^{-2}) under optimal operating condition (U_c = 9 kV, U_p = 20 kV), the total energy consumption is 23.33 W m^{-2}.

To rationalize the filter's behavior across different air velocities on a meaningful timescale, the clean air delivery rate (CADR) was calculated as CADR = $\eta \times Q$, where η is the filtration efficiency and Q is the volumetric flow rate. As summarized in Supplementary **Fig. S6**, CADR increases monotonically with air velocity, despite the decrease in η, because the increase in volumetric throughput dominates. The energy consumption (including power supplies and fan) per unit CADR decreases with increasing air velocity, indicating that higher flow rates improve energy utilization efficiency in terms of clean air output. An quantitative energy consumption data was added in Supplementary **Table S1**. As shown in **Table S1**, the total energy consumption of our filtration system is 0.060 Wh m^{-3} (CADR-normalized), compared to 0.138 Wh m^{-3} for conventional filtration under equivalent conditions. Particle charging (9 kV) and filter polarization (20 kV) account for 40.5% and 58.6% of total power input, respectively. Despite the use of high voltages, the system remains energy-competitive with conventional approaches on a per-CADR basis, owing to the significant enhancement in filtration efficiency enabled by electrostatic assistance.

Long-term performance was conducted at U_c = 9 kV, U_p = 20 kV, and an air velocity of 0.053 m s^{-1} for 240 h. Experiments were conducted under real environmental conditions, with temperature ranging from 20.4 °C to 23.9 °C and relative humidity from 42.0% to 72.6%. It should be noted that rGO is thermodynamically metastable, and its reduction state may gradually evolve under such ambient temperature and humidity fluctuations [43–45], representing an inherent limitation of rGO-based materials that warrants attention in long-term deployment. Detailed environmental parameters are provided in Supplementary **Fig. S7**. As shown in Fig. 9a, the filtration efficiency for 0.3–0.5, 0.5–1, and 1–3 μm PM remained high, averaging 99.55%, 99.37%, and 98.77%, respectively. As shown in Fig. 9b, the pressure drop remained basically unchanged, fluctuating between 1.3 and 1.5 Pa with an average value of 1.4 Pa. This stability is attributed to the large pore size (>200 μm, Fig. 4d) relative to the particle diameter (0.3–3 μm) and the low indoor PM concentration used in testing (Supplementary **Fig. S1b**), which together prevent pore blockage. The sustained high efficiency and nearly unchanged low pressure drop suggest a high dust-holding capacity and a potentially long service life of the PDA/rGO@PET-2.5 min filter.

In order to evaluate the anti-detachment performance of the filter, a cyclic durability test consisting of 10 consecutive steps of filtration, washing, drying, and re-testing was conducted. In the washing step, each filter sample underwent four deionized water wash followed by one ethanol wash to remove any loosely bound GO/rGO. With the exception of the 4th, 7th, and 10th washing cycle, which was conducted by ultrasonication for 5 min at 40 kHz, the preceding cycles are all performed manually. As shown in Supplementary **Fig. S8**, the PDA/rGO@PET-2.5 min filter maintained an average filtration efficiency of 99.70% for 0.3–0.5 μm PM at 0.053 m s^{-1} across all 10 cycles, with the pressure drop remaining consistently at ~1.4 Pa throughout. The absence of any statistically significant degradation in either filtration efficiency or pressure drop across all 10 cycles confirms that the PDA and rGO coating is firmly anchored to the PET fiber surface and does not detach under repeated use and washing conditions, indicating little risk of secondary contamination from coating detachment.

We summarized the comprehensive performance of the reported electrostatic filters, non-electret filters and this work at the same air velocity of 0.053 m s^{-1} in Supplementary **Table S2** and Fig. 9c. Non-electret filters can achieve high filtration efficiency but typically at the

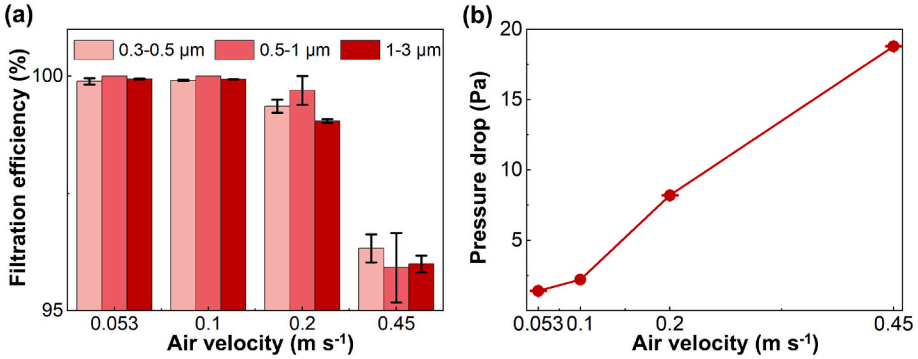

Fig. 8. Filtration performance of the EAA PDA/rGO@PET-2.5 min filter at different air velocities. (a) Filtration efficiency for 0.3–3 μm PM at different air velocities when U_c = 9 kV and U_p = 20 kV. Error bars represent the SE from four independent measurements. (b) pressure drop at different air velocities when U_c = 9 kV and U_p = 20 kV. Error bars represent the SE from five independent measurements.

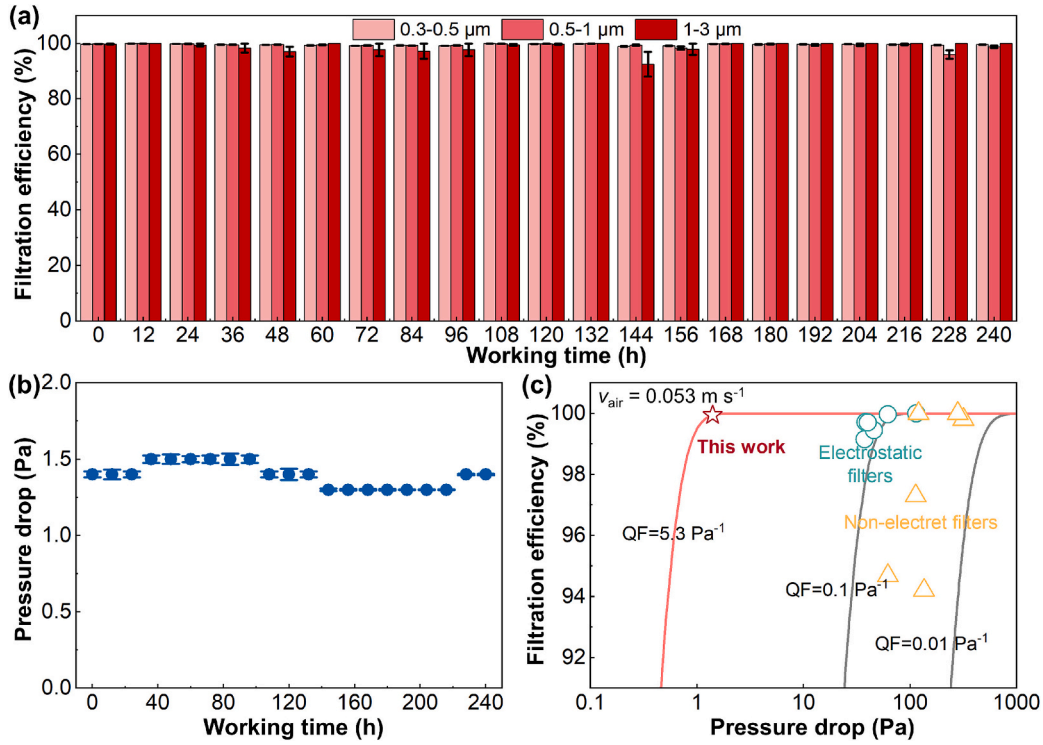

Fig. 9. Long-term performance of the PDA/rGO@PET-2.5 min filter when $U_c = 9$ kV and $U_p = 20$ kV, including (a) filtration efficiency for 0.3–3 μm PM at 0.053 m s^{-1}. Error bars represent the SE from four independent measurements. And (b) pressure drop at 0.053 m s^{-1}. Error bars represent the SE from five independent measurements. (c) The performance comparison of reported electrostatic filters (green dots), non-electret filters (yellow triangles) and the PDA/rGO@PET filters (red stars) in this work. All filtration efficiencies are for 0.3–0.5 μm PM and all pressure drops are tested at ~0.053 m s^{-1} air velocity. Detailed information is provided in Supplementary Table S2. (For interpretation of the references to color in this figure legend, the reader is referred to the web version of this article.)

expense of a high pressure drop. Electrostatic filters have low pressure drop, but often exhibit lower filtration efficiency, which can be improved. This work achieves high filtration efficiency (99.94% for 0.3–0.5 μm PM) while maintaining extremely low pressure drop (1.4 Pa), therefore contributing to an extremely high QF of 5.3 Pa^{-1}, one order of magnitude higher than reported electrostatic filters and non-electret filters. It should be noted that QF is a composite metric that balance efficiency against pressure drop. In applications where a minimum filtration efficiency is mandatory (such as medical, pharmaceutical, or cleanroom environments) these metrics should be interpreted alongside the absolute filtration efficiency values rather than in isolation.

4. Conclusions

This study demonstrates a PDA-mediated GO/rGO surface modification route that improves filtration efficiency without sacrificing the intrinsic low pressure drop of PET coarse filters. *In situ* PDA/GO coating followed by controlled HI-vapor reduction yields a uniform PDA/rGO layer on PET fibers while preserving the open fibrous architecture. More importantly, we found the GO reduction time should be carefully optimized to balance two competing effects: a sufficiently high ε_r to promote dielectric polarization and enhance electrostatic particle capture, and a sufficiently low electrical conductivity to prevent electric-field shielding within the fibrous network. The electric-field shielding can weaken the electric field inside the filter, whereas a 2.5 min reduction yields the best filtration performance. Under $U_c = 9$ kV and $U_p = 20$ kV, the optimized PDA/rGO@PET-2.5 min filter achieved up to 99.94% filtration efficiency for 0.3–0.5 μm PM with an ultralow pressure drop of 1.4 Pa at an air velocity of 0.053 m s^{-1}. This filter demonstrated stably high filtration efficiency and low pressure drop during a 240-h continuous operation. The mechanism and methodology proposed in this study offer a promising pathway toward energy-efficient filtration systems. We acknowledge that the proposed electric-field shielding mechanism is currently inferred from experimental observations, and that ε_r enhancement may not be the sole contributor to the efficiency improvement. Future work should aim to quantify in-filter electric-field distributions through simulations or *in situ* measurements, perform charge distribution analysis, and validate robustness under broader environmental and aerosol conditions. Additionally, systematic long-term stability testing under controlled temperature and humidity conditions is needed to quantitatively assess how aging-induced changes in the reduction state of rGO affect filtration performance and service lifetime.

Declaration of competing interest

The authors declare that they have no known competing financial interests or personal relationships that could have appeared to influence the work reported in this paper.

Acknowledgments

The research was supported by the National Natural Science Foundation of China (Nos. 52408122, 52325801 and U25A20341).

Appendix A. Supplementary data

Supplementary data to this article can be found online at https://doi.org/10.1016/j.seppur.2026.138974.

Data availability statement

The data supporting this study's findings are available in the paper

and in the Supplementary Materials. Additional data are available from the corresponding authors upon request.

References

[1] V.A. Southerland, M. Brauer, A. Mohegh, M.S. Hammer, A. van Donkelaar, R. V. Martin, J.S. Apte, S.C. Anenberg, Global urban temporal trends in fine particulate matter ($PM_{2.5}$) and attributable health burdens: estimates from global datasets, Lancet Planet. Health 6 (2) (2022) e139–e146.

[2] N. Liu, W. Liu, F. Deng, Y. Liu, X. Gao, L. Fang, Z. Chen, H. Tang, S. Hong, M. Pan, W. Liu, X. Huo, K. Guo, F. Ruan, W. Zhang, B. Zhao, J. Mo, C. Huang, C. Su, C. Sun, Z. Zou, H. Li, Y. Sun, H. Qian, X. Zheng, X. Zeng, J. Guo, Z. Bu, C. Mandin, O. Hänninen, J.S. Ji, L.B. Weschler, H. Kan, Z. Zhao, Y. Zhang, The burden of disease attributable to indoor air pollutants in China from 2000 to 2017, Lancet Planet. Health 7 (11) (2023) e900–e911.

[3] X. Bu, Z. Xie, J. Liu, L. Wei, X. Wang, M. Chen, H. Ren, Global PM2.5-attributable health burden from 1990 to 2017: estimates from the global burden of disease study 2017, Environ. Res. 197 (2021) 111123.

[4] M. Stafoggia, B. Oftedal, J. Chen, S. Rodopoulou, M. Renzi, R.W. Atkinson, M. Bauwelinck, J.O. Klompmaker, A. Mehta, D. Vienneau, Z.J. Andersen, T. Bellander, J. Brandt, G. Cesaroni, K. de Hoogh, D. Fecht, J. Gulliver, O. Hertel, B. Hoffmann, U.A. Hvidtfeldt, K.-H. Jöckel, J.T. Jørgensen, K. Katsouyanni, M. Ketzel, D.T. Kristoffersen, A. Lager, K. Leander, S. Liu, P.L.S. Ljungman, G. Nagel, G. Pershagen, A. Peters, O. Raaschou-Nielsen, D. Rizzuto, S. Schramm, P. E. Schwarze, G. Severi, T. Sigsgaard, M. Strak, Y.T. van der Schouw, M. Verschuren, G. Weinmayr, K. Wolf, E. Zitt, E. Samoli, F. Forastiere, B. Brunekreef, G. Hoek, N.A. H. Janssen, Long-term exposure to low ambient air pollution concentrations and mortality among 28 million people: results from seven large European cohorts within the ELAPSE project, Lancet Planet. Health 6 (1) (2022) e9–e18.

[5] H. Yin, E.E. McDuffie, R.V. Martin, M. Brauer, Global health costs of ambient $PM_{2.5}$ from combustion sources: a modelling study supporting air pollution control strategies, Lancet Planet. Health 8 (7) (2024) e476–e488.

[6] N.E. Klepeis, W.C. Nelson, W.R. Ott, J.P. Robinson, A.M. Tsang, P. Switzer, J. V. Behar, S.C. Hern, W.H. Engelmann, The National Human Activity Pattern Survey (NHAPS): a resource for assessing exposure to environmental pollutants, J. Expo. Sci. Environ. Epidemiol. 11 (3) (2001) 231–252.

[7] Z. Li, J. Luo, H. Yang, Corrosion-resistant amino acid-based deep eutectic solvents toward liquid desiccant air conditioning systems, Energy Use 1 (1) (2025) 100004.

[8] A. Afshari, G. Hultmark, Toward individual thermal comfort and energy saving in open plan offices with chilled beams, Energy Use 1 (2) (2025) 100029.

[9] C. Yao, S. Lee, X. Wen, J. Lee, S. Lee, S. Choi, D. Huh, T. Kim, A numerical study on effective arrangement of fan-filter units in a semiconductor cleanroom: control of hazardous gas leakage from a process instrument, Build. Environ. 267 (2025) 112301.

[10] W.C. Hinds, Y. Zhu, Aerosol Technology: Properties, Behavior, and Measurement of Airborne Particles, John Wiley & Sons, 2022.

[11] C.-Y. Tien, J.-P. Chen, S. Li, Z. Li, Y.-M. Zheng, A.S. Peng, F. Zhou, C.-J. Tsai, S.-C. Chen, Experimental and theoretical analysis of loading characteristics of different electret media with various properties toward the design of ideal depth filtration for nanoparticles and fine particles, Sep. Purif. Technol. 233 (2020) 116002.

[12] A. Toptas, M.D. Calisir, M. Gungor, A. Kilic, Enhancing filtration performance of submicron particle filter media through bimodal structural design, Polym. Eng. Sci. 64 (2) (2024) 901–912.

[13] E. Tian, Q. Chen, Y. Gao, Z. Chen, Y. Wang, J. Mo, Advancing indoor air purification by mass transfer enhancement: bridging the gap between high-performance materials and technologies, Engineering (2025), https://doi.org/10.1016/j.eng.2025.07.003.

[14] E. Tian, Y. Gao, J. Mo, Experimental studies on electrostatic-force strengthened particulate matter filtration for built environments: Progress and perspectives, Build. Environ. 228 (2023) 109782.

[15] E. Tian, J. Mo, Toward energy saving and high efficiency through an optimized use of a PET coarse filter: the development of a new electrostatically assisted air filter, Energ. Buildings 186 (2019) 276–283.

[16] E. Tian, F. Xia, J. Wu, Y. Zhang, J. Li, H. Wang, J. Mo, Electrostatic air filtration by multifunctional dielectric heterocaking filters with ultralow pressure drop, ACS Appl. Mater. Interfaces 12 (26) (2020) 29383–29392.

[17] Y. Gao, E. Tian, J. Mo, Electrically responsive coarse filters endowed by high-dielectric-constant surface coatings toward efficient removal of ultrafine particles and ozone, ACS ES&T Eng. 1 (10) (2021) 1449–1459.

[18] D.-H. Kim, M.-J. Kim, S.-Y. Kwak, J. Jeong, D. Choi, S.W. Choi, J. Ryu, K.-S. Kang, Bioengineered liver crosslinked with nano-graphene oxide enables efficient liver regeneration via MMP suppression and immunomodulation, Nat. Commun. 14 (1) (2023) 801.

[19] H. Yu, Y. He, G. Xiao, Y. Fan, J. Ma, Y. Gao, R. Hou, X. Yin, Y. Wang, X. Mei, The roles of oxygen-containing functional groups in modulating water purification performance of graphene oxide-based membrane, Chem. Eng. J. 389 (2020) 124375.

[20] D. Maurya, S. Khaleghian, R. Sriramdas, P. Kumar, R.A. Kishore, M.G. Kang, V. Kumar, H.-C. Song, S.-Y. Lee, Y. Yan, J.-M. Park, S. Taheri, S. Priya, 3D printed graphene-based self-powered strain sensors for smart tires in autonomous vehicles, Nat. Commun. 11 (1) (2020) 5392.

[21] C. Han, J. Jiang, L. Mu, W. Zhao, J. Liu, J. Lan, S. Hu, H. Yang, S. Gao, F. Zhou, J. Chen, Y. Fan, X. Duan, P. Li, L. Chen, Quasi-vertically asymmetric channels of graphene oxide membrane for ultrafast ion sieving, Nat. Commun. 16 (1) (2025) 1020.

[22] X. Zhu, E. Tian, Z. Li, D. Xie, Q. Shao, Z. Sun, R. Li, E. Wang, K. Liu, K. Liu, Graphene oxide-carbon nanotube hybrid membranes for high-pressure and high-flux nanofiltration, Adv. Funct. Mater. 35 (45) (2025) 2503432.

[23] H. Sun, L. Mei, J. Liang, Z. Zhao, C. Lee, H. Fei, M. Ding, J. Lau, M. Li, C. Wang, X. Xu, G. Hao, B. Papandrea, I. Shakir, B. Dunn, Y. Huang, X. Duan, Three-dimensional holey-graphene/niobia composite architectures for ultrahigh-rate energy storage, Science 356 (6338) (2017) 599–604.

[24] E. Prokhorov, Z. Barquera-Bibiano, A. Manzano-Ramírez, G. Luna-Barcenas, Y. Kovalenko, M.A. Hernández-Landaverde, B.E.C. Reyes, J.H. Vargas, New insights in graphene oxide dielectric constant, Mater. Res. Express 6 (8) (2019) 085622.

[25] L.J. Romasanta, M. Hernández, M.A. López-Manchado, R. Verdejo, Functionalised graphene sheets as effective high dielectric constant fillers, Nanoscale Res. Lett. 6 (1) (2011) 508.

[26] K. Deshmukh, M.B. Ahamed, S.K. Pasha, R.R. Deshmukh, P.R. Bhagat, Highly dispersible graphene oxide reinforced polypyrrole/polyvinyl alcohol blend nanocomposites with high dielectric constant and low dielectric loss, RSC Adv. 5 (76) (2015) 61933–61945.

[27] S. Roh, K. Park, J. Kim, Design of web-to-web spacing for the reduced pressure drop and effective depth filtration, Polymers 11 (11) (2019) 1822.

[28] E. Tombácz, I.Y. Tóth, K. Kovács, E. Illés, M. Szekeres, B. Barna, A. Csicsor, T. Szabó, Striking analogies and dissimilarities between graphene oxides and humic acids: pH-dependent charging and colloidal stability, J. Mol. Liq. 306 (2020) 112948.

[29] H. Frost, T. Bond, T. Sizmur, M. Felipe-Sotelo, Sorption of metal ions onto PET-derived microplastic fibres, Environ. Sci. Process Impacts 26 (12) (2024) 2309–2319.

[30] H. Lee, S.M. Dellatore, W.M. Miller, P.B. Messersmith, Mussel-inspired surface chemistry for multifunctional coatings, Science 318 (5849) (2007) 426–430.

[31] N. Bonanos, P. Pissis, J.R. Macdonald, Impedance spectroscopy of dielectrics and electronic conductors, Charact. Mater. (2012) 1–14.

[32] E. Tian, J. Mo, Z. Long, H. Luo, Y. Zhang, Experimental study of a compact electrostatically assisted air coarse filter for efficient particle removal: synergistic particle charging and filter polarizing, Build. Environ. 135 (2018) 153–161.

[33] K.J. Boelter, J.H. Davidson, Ozone generation by indoor, electrostatic air cleaners, Aerosol Sci. Technol. 27 (6) (1997) 689–708.

[34] E. Tian, Y. Gao, J. Mo, Electrostatically assisted air coarse filtration for energy efficient ambient particles removal: Long-term performance in real environment and influencing factors, Build. Environ. 164 (2019) 106348.

[35] GB/T 14295–2019, Air Filter, Standardization Administration of the People's Republic of China, Beijing, China, 2019, https://openstd.samr.gov.cn/bzgk/std/newGbInfo?hcno=66FD4006FD45C7D58D9F021C52E8222D.

[36] C.-S. Wang, Electrostatic forces in fibrous filters—a review, Powder Technol. 118 (1–2) (2001) 166–170.

[37] R.C. Brown, Capture of dust particles in filters by linedipole charged fibres, J. Aerosol Sci. 12 (4) (1981) 349–356.

[38] Y. Gao, E. Tian, Y. Zhang, J. Mo, Utilizing electrostatic effect in fibrous filters for efficient airborne particles removal: principles, fabrication, and material properties, Appl. Mater. Today 26 (2022) 101369.

[39] Y. Liu, Z. Ning, Y. Chen, M. Guo, Y. Liu, N.K. Gali, L. Sun, Y. Duan, J. Cai, D. Westerdahl, X. Liu, K. Xu, K.-F. Ho, H. Kan, Q. Fu, K. Lan, Aerodynamic analysis of SARS-CoV-2 in two Wuhan hospitals, Nature 582 (7813) (2020) 557–560.

[40] GB/T 13554–2020, High Efficiency Particulate Air Filter, Standardization Administration of the People's Republic of China, Beijing, China, 2020, https://openstd.samr.gov.cn/bzgk/std/newGbInfo?hcno=20DD54075DA2574DF6789D622789275A.

[41] JG/T 404–2013,, Air Filter Media, Ministry of Housing and Urban-Rural Development of the People's Republic of China, Beijing, China, 2013, https://std.samr.gov.cn/hb/search/stdHBDetailed?id=8B1827F1937DBB19E05397BE0A0AB44A.

[42] Y. Gao, Y. Gu, E. Tian, J. Mo, A two-stage cascaded ionizer for boosting PM charging in electrostatic filtration: principles, design, and long-term performance, Sep. Purif. Technol. 313 (2023) 123494.

[43] O.Ö. Ekiz, M. Ürel, H. Güner, A.K. Mizrak, A. Dâna, Reversible electrical reduction and oxidation of graphene oxide, ACS Nano 5 (4) (2011) 2475–2482.

[44] A. Hunt, D.A. Dikin, E.Z. Kurmaev, T.D. Boyko, P. Bazylewski, G.S. Chang, A. Moewes, Epoxide speciation and functional group distribution in graphene oxide paper-like materials, Adv. Funct. Mater. 22 (18) (2012) 3950–3957.

[45] F. Zhao, L. Wang, Y. Zhao, L. Qu, L. Dai, Graphene oxide nanoribbon assembly toward moisture-powered information storage, Adv. Mater. 29 (3) (2017) 1604972.